J Mater Sci: Mater Med (2011) 22:1195–1203
DOI 10.1007/s10856-011-4297-4

Evaluation of 3D nano–macro porous bioactive glass scaffold for hard tissue engineering

S. Wang · M. M. Falk · A. Rashad ·
M. M. Saad · A. C. Marques · R. M. Almeida ·
M. K. Marei · H. Jain

Received: 29 September 2010 / Accepted: 16 March 2011 / Published online: 29 March 2011

Abstract Recently, nano–macro dual-porous, three-dimensional (3D) glass structures were developed for use as bioscaffolds for hard tissue regeneration, but there have been concerns regarding the interconnectivity and homogeneity of nanopores in the scaffolds, as well as the cytotoxicity of the environment deep inside due to limited fluid access. Therefore, mercury porosimetry, nitrogen absorption, and TEM have been used to characterize nanopore network of the scaffolds. In parallel, viability of MG 63 human osteosarcoma cells seeded on scaffold surface was investigated by fluorescence, confocal and electron microscopy methods. The results show that cells attach, migrate and penetrate inside the glass scaffold with high proliferation and viability rate. Additionally, scaffolds were implanted under the skin of a male New Zealand rabbit for in vivo animal test. Initial observations show the formation of new tissue with blood vessels and collagen fibers deep inside the implanted scaffolds with no obvious inflammatory reaction. Thus, the new nano–macro dual-porous glass structure could be a promising bioscaffold for use in regenerative medicine and tissue engineering for bone regeneration.

S. Wang · H. Jain (✉)
Department of Materials Science and Engineering,
Lehigh University, Bethlehem, PA, USA
e-mail: H.Jain@Lehigh.Edu

M. M. Falk
Department of Biological Sciences, Lehigh University,
Bethlehem, PA, USA

A. Rashad · M. M. Saad · M. K. Marei
Tissue Engineering Laboratories, Faculty of Dentistry,
Alexandria University, Alexandria, Egypt

A. C. Marques
Departamento de Engenharia de Materiais/ICEMS,
Instituto Superior Técnico/TULisbon, Lisbon, Portugal

R. M. Almeida
Departamento de Engenharia Química e Biológica/ICEMS,
Instituto Superior Técnico/TULisbon, Lisbon, Portugal

1 Introduction

With the increase of life expectancy, the demand of bone tissue replacement has been expanding [1]. Nowadays, two main strategies are used to replace the dysfunctional tissues: transplantation and implantation. In spite of the success of transplantation, the number of donors is limited and there are potential risks of disease transmission. To solve these limitations, instead of transplantation, the dysfunctional tissues can be repaired by using implants made from biomaterials [2]. Bioactive materials, e.g. bioactive ceramics and bioactive glass (BG), which can facilitate direct interfacial bonds between implant and tissue without scar tissue formation as contrast to conventional biomaterials, e.g. titanium and cobalt-chrome alloys, have been widely studied and used [3, 4]. However, the bulk bioactive ceramics, like hydroxyapatite, and BGs usually do not degrade rapidly enough and may remain in the human body for a long time [5]. A different approach to the treatment has been proposed based on tissue engineering: rather than providing an implant as a replacement for the diseased tissue, a scaffold is implanted. An ideal bioscaffold would not only provide a three dimensional (3D) structure to facilitate the regeneration of natural tissue, but also degrade gradually and, eventually be replaced by the natural tissue completely [6].

A few criteria have been proposed for an ideal bioscaffold, including biocompatibility, biodegradation, high porosity and hundreds of microns size pores to allow tissue ingrowth, blood vessel formation, and nutrient delivery to the newly formed tissue [7–12]. Various techniques have been developed to generate the porous bioactive ceramic/BG scaffolds, including polymer foam replica method [13–16], three dimensional printing [17, 18], dry press method [19–22], freeze cast [23] and glass fiber sintering [24]. In most of these synthesis methods, micron size particles of melt-quench derived BG were used as the starting material and only macropores at micron level were produced. In this regard, there is evidence that the nanostructure of biomaterials may provide both physical and chemical advantages to guide cell attachment, migration and differentiation [25–27]. Furthermore, nanopores can be used to tailor the degradation process of the scaffold, since they dramatically increase the surface area. Therefore, it seems beneficial to incorporate nanopores into bioscaffolds. Since nanopores are inherent to the sol–gel method of glass fabrication, sol–gel derived materials have been investigated for potential bioscaffolds. For example, Jones et al. produced bioscaffolds by foaming a sol–gel derived BG [28]. While the pore size can be fairly large using the foaming method, it is difficult to maintain high interconnectivity between the macropores. Therefore, we recently fabricated coral-like tailored amorphous multi-porous (TAMP) bioscaffolds by combining the sol–gel process with spinodal decomposition, and then achieved high interconnectivity as well as large macropores at >100 μm scale [29–31].

Although highly promising, concerns regarding the cytotoxicity of the nano–macro porous BG scaffolds remain [32]. Excessively high ion concentration in the local fluid environment around bone cells is suspected to be the cause of cytotoxicity [33]. Presumably, the pores inside the scaffolds, which have limited fluid access, may reach ion concentrations large enough to become cytotoxic. At the same time, homogeneity and interconnectivity of nanopores in scaffolds has not been fully characterized and understood. To assess these concerns, in this study, we have synthesized and characterized sol–gel derived bioscaffolds, especially nanopores of the scaffolds, and investigated bone cell's in vitro and animal tissue's in vivo response to this novel nano–macro porous 3D structure.

2 Materials and methods

We selected 70 mol% SiO_2–30 mol% CaO composition, referred to as 70S30C in the literature, for fabricating 3D nano–macro porous bioactive glass scaffold samples as described in detail previously [29]. Briefly, polyethylene oxide (PEO) was dissolved into 0.05 N acetic acid solution, to which tetramethyl orthosilicate (TMOS) and calcium nitrate tetrahydrate $Ca(NO_3)_2 \cdot 4H_2O$ were added. After vigorous stirring for 10 min, 2.5 vol% HF (a gelation catalyst) was added, and then the sol was cast into wells of tissue culture plates. Samples were aged at 40°C for 1 day, and then soaked in ammonia solution for 3 days before they were dried and thermally stabilized at 700°C.

The interconnected pore size distribution of the specimens was determined by mercury porosimetry using intrusion curve. Specimens were dried at 150°C for 2 h before testing in an AutoPore IV 9500 porosimeter (Micromeritics, Norcross, GA). Specific surface area and nano porosity in the gel skeleton were determined by nitrogen adsorption (ASAP 2020, Micromeritics, Norcross, GA) BET [34] and BJH methods [35] using adsorption and desorption curves, respectively. For these experiments, accurately weighed specimens were evacuated and heated at 350°C for at least 5 h to remove moisture and potential surface contaminants before analysis.

MG63 osteoblast-like cells (ATCC, CRL-1427) were chosen as the model to study cell response to our samples. Cells were cultured in 6 cm tissue culture dishes and maintained in an incubator at 37°C, 5% CO_2, 95% air and saturated humidity. Dulbecco's Modified Eagle Medium (DMEM) supplemented with 10% fetal bovine serum (FBS) and 1% penicillin/streptomycin was used as complete culture medium. Cells were subcultured upon confluency.

Before cell seeding, samples were soaked in 70% ethanol twice, 5 min each time, followed by soaking in water for 5 min, air dried for at least half hour, sterilized under ultraviolet light for 10 min, and presoaked in complete culture medium for 30 min. Cells, then, were harvested from tissue culture dishes and seeded on the samples, at density of 120 cells/mm^2. The samples were submerged in complete culture medium to ensure nutrient delivery to cells on surface. Cellular observations were made 48 h post seeding.

For fluorescence and confocal imaging, a LIVE/DEAD® Viability/Cytotoxicity Kit (Molecular Probes, Invitrogen, Carlsbad, CA) was used to stain and quantify cell-viability by following manufacturer's instructions. Alternatively, cytoskeletal F-actin filaments and cell nuclei were stained with Alexa488-Phalloidin (green) and Propidium Iodide (red) (Invitrogen, Carlsbad, CA) after fixation of cells on the scaffolds in 4% formaldehyde for 15 min at room temperature. Specimens were examined by fluorescence (Nikon Eclipse TE200U) and confocal microscopy (Zeiss LSM 510).

For scanning electron microscopy (SEM) examination, porous glass specimens were mounted on SEM stubs using colloidal graphite and coated with a thin iridium metal film by sputtering. Specimens were imaged with an environmental SEM (Phillips, XL-30) using a relatively low accelerating voltage of 5 kV. For imaging of cells grown on glass scaffolds, samples were removed from tissue culture plates, rinsed in 0.1 M phosphate buffer solution, fixed in 0.1 M phosphate buffer supplemented with 3% glutaraldehyde (w/v), rinsed in 0.1 M phosphate buffer, followed by stepwise dehydration in a graded series of ethanol (35%, 60%, 80%, 95%, 95%, and 100%). After drying with hexamethyldisilazane (HMDS, Sigma), samples were coated with iridium and examined as described above.

To investigate the nanopore network, samples were examined by transmission electron microscopy (TEM). The porous glass powders were collected by scraping scaffolds with a razor blade, mixed with ethanol (200 proof, absolute, anhydrous) and ground for 5 minutes. A drop of the glass-powder/ethyl alcohol suspension was transferred onto a lacey carbon-coated 300 mesh copper grid (SPI# 3830C-FA), and after air-drying for 10–15 min was loaded into the TEM (Philips EM 420T) specimen chamber and examined with an electron accelerating voltage of 100 kV.

For animal in vivo test, four discs of 1 cm diameter and ~5 mm thickness were prepared and sterilized by autoclave for surgical implantation in a white New Zealand male rabbit. Guidelines for the care and use of laboratory animals were followed in all experiments [36]. General anesthesia was administered using Xylazine HCL 2% in a dose of 20 mg/kg body weight followed by ketamine HCL in a dose of 100 mg/kg body weight intra-peritoneal. Four subcutaneous pouches were created on the dorsal surface of the animal, with a distance of approximately 2 cm between pouches. The prepared discs were implanted in the pouches that were made just to encompass the disc scaffold, and shallow enough to maintain the underlying fascia intact. The wounds were then sutured using 3.0 silk suture material [37].

At 5 weeks post-surgery, full thickness specimens including the implants were excised, immediately placed in 10% formalin fixative, and stepwise dehydrated in graded concentrations of ethyl alcohol. Specimens were cleaned in xylene, followed by embedding in methyl methacrylate resin (Aldrich) for histological hard section preparation. Then they were stained with Stevenel's blue (connective tissue stained bluish-green) and Van Gieson's stains (hard tissue stained red) (Bio-Optica, Milano, Italy) [38]. Sections were examined and photographed by a light microscope (Olympus model CH40, Tokyo, Japan).

3 Results

A typical BG scaffold sample with the mould shape is shown in Fig. 1. Various shapes of scaffold can be readily achieved by casting the sol into appropriate moulds. In our synthesis method, polymer induced spinodal decomposition was introduced to fabricate the highly-interconnected coral-like macro-structure. The interconnected macropores in our BG scaffolds can be seen clearly in SEM images (Fig. 2), as well as in mercury porosimetry data (Fig. 3a). Nanopores, with a diameter ranging from several to tens of nanometers (with the peak value at 20–30 nm), coexist with the macropores (tens to one hundred microns in diameter) in the BG scaffold.

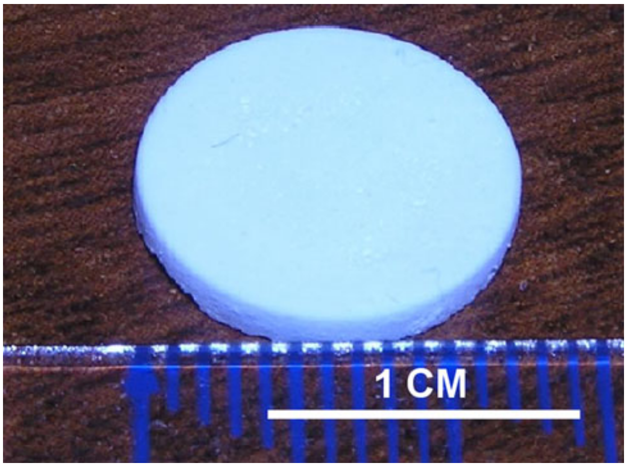

Fig. 1 A representative nano–macro porous BG scaffold derived from casting the sol into a well of a tissue culture plastic plate

In addition, nanopores in the scaffolds were characterized by mercury porosimetry, nitrogen adsorption and TEM. The nanopore size distributions measured by mercury porosimetry (Fig. 3a) and nitrogen adsorption (Fig. 3b) are in good agreement. The volume of the nanopores (<100 nm) contributes ~24% to the total porosity. Furthermore, TEM has provided direct observation of the nanopore morphology. Typical/representative bright field TEM micrographs of our porous glass samples are shown in Fig. 4. There are some cloudy grains inside the gel matrix with interconnected lighter channels in between.

Nanopores with diameter in several nanometers are inherent to the sol–gel fabrication process [39]. Furthermore, the nanopore size can be enlarged from several to tens of nanometers by solvent exchange process [40, 41]. The mechanism of this process has been proposed by Nakanishi et al. [42]: When the gel is soaked in a basic solvent at a distinct temperature, the wet sample on the positive curvature dissolves, followed by reprecipitation onto the part with negative curvature by the so-called Ostwald ripening process. This process results in the condensation of intra-domains and therefore, larger inter-domain pores [16]. In our case, ammonia was used in this solvent exchange process to enlarge the nanopore size. It helped enlarge the nanopores from 6 nm to 22 nm without

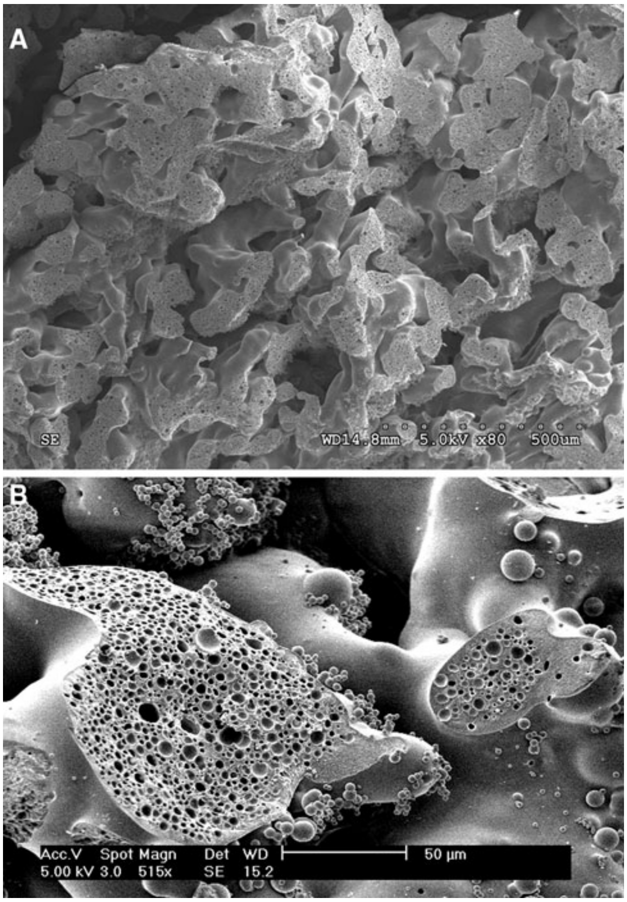

Fig. 2 SEM images of BG scaffold **a** in low magnification and **b** in higher magnification

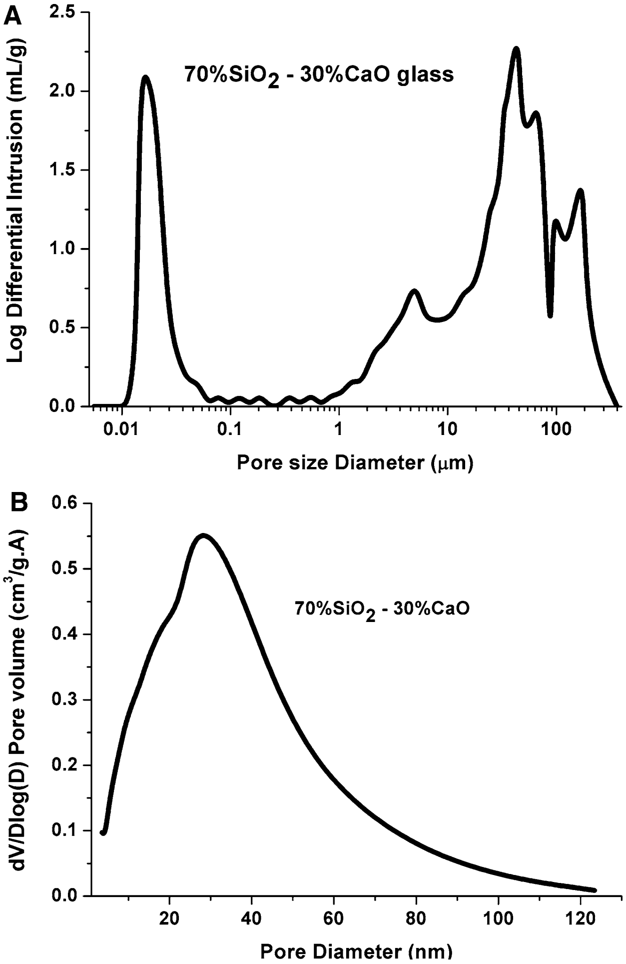

Fig. 3 Interconnected macropore size distribution from **a** mercury intrusion porosimetry and **b** mesopore size distributions from nitrogen adsorption analysis

significantly affecting the macro pores [31]. However, there had been concern about the homogeneity of these enlargement effects due to the limited accessibility of ammonia deep inside the scaffolds. To address this concern, two specimens from the same sample were examined: one from the sample surface and another from the center of the sample. The images shown in Fig. 4 demonstrate that no significant structural difference is observed between the two specimens, indicating that the ammonia solution is able to penetrate through the macropores (at micron level, shown in Fig. 2) into the glass scaffold and to enlarge the nanopores deep in the interior. Thus, the nanopore network is homogeneous throughout the sample.

MG63 osteoblast-like cells growing on the BG scaffolds are shown in Fig. 5. Live cells (green) are distinguished from dead cells (red) as a result of Live/Dead, Viability/Cytotoxicity staining. To examine whether cells would penetrate into the interior of 3D scaffold, or only colonize/survive on its surface, scaffolds are examined by z-serial confocal microscopy. Images were acquired at different depths ranging from 0 to 500 µm from the surface using a 40× magnification oil-immersion lens (NA 1.2, Zeiss, PlanFluor). Representative sections shown in Fig. 5 demonstrate that the cells exhibit a high viability throughout the entire depth of the scaffolds examined. To investigate cell morphology in greater detail, fixed samples were stained with Alexa488-Phalloidin (green) for observing cytoskeletal F-actin filaments, and with Propidium Iodide (red) for examining cell nuclei, and examined at higher primary magnification (63× oil immersion lens, NA1.4, Zeiss PlanAppochromat). Representative images and 3D-volume reconstructions shown in Fig. 6 show well-spread cells with a flattened morphology, supporting good adhesion of the MG63 cells to the highly contoured 3D-scaffold surface.

To further confirm that cells actively penetrated the glass scaffold and colonized it deeply inside, and not just adhered to its surface, BG scaffolds colonized by cells for 2 days were cross-sectioned, fixed, dehydrated

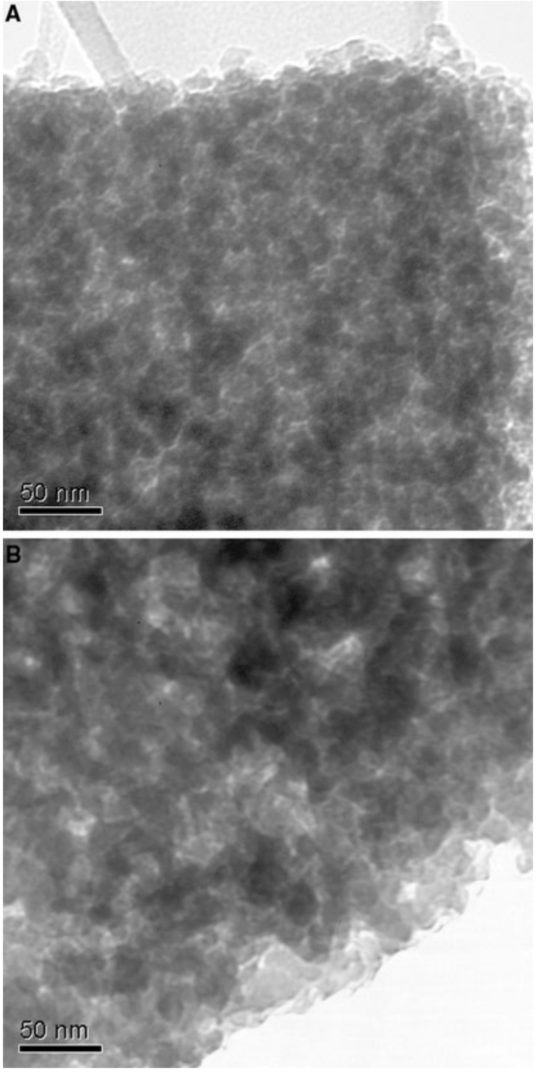

Fig. 4 Bright field TEM micrographs of specimen from **a** near the surface and **b** at the center of sample

and investigated by SEM. A cross-section view from 1 mm under the cell-seeding surface is shown in Fig. 7, which indicates epitheloid, well-spread, flattened cell morphology.

In vivo response of animal tissue was examined at 5 weeks post-surgery. The operated rabbit skin area appears normal with grown hair under macroscopic observation. Upon histological examination of the specimens, a thin fibrous capsule surrounding the implanted scaffold is observed as a regular tissue reaction to the inserted biomaterial. The capsule is integrated with the surrounding tissues showing heavily distributed new blood vessels without visible inflammatory reaction (Fig. 8a). The histological micrographs also demonstrate collagen fiber strands growing and extending from the boundaries of the capsule to invade the core of the scaffold (Fig. 8b).

4 Discussion

For an ideal scaffold, high interconnectivity between macropores is desired for tissue ingrowth and blood vessel formation. However, it is difficult to achieve highly interconnected macropores using some of current synthesis methods [28]. Therefore, we used spinodal decomposition method to create interconnected macroporous structures. Basically, repulsive interaction between the solvent and the PEO molecules adsorbed on silica oligomers leads to spinodal phase separation, one phase rich in PEO and silica and the other phase rich in solvent [43]. These two phases interpenetrate each other, resulting in highly interconnected coral-like macrostructure. Therefore, in comparison to the spherical pores created by foaming method [28], the polymer induced spinodal decomposition can generate highly interconnected macro-structure as seen in Fig. 2.

Besides the macrostructure, it is also important to introduce nanopores, which form inherently during the sol–gel process, to manipulate biodegradability and enhance bioactivity. The nanostructure evolution during the sol–gel process in 70S30C glass, the composition we used here, has been studied by Lin et al. [44]. They suggested that in the sols before gelling, TEOS hydrolyzes and poly-condensates into primary particles, which then aggregate into bigger particles, the so-called secondary particles during the gelling and drying process. These secondary particles then fuse into tertiary particles during the heat treatment. In our study, the nanopores result from the interstitial space between these tertiary particles, which appear as cloudy grains in our TEM images (Fig. 4).

The nanopore volume can be measured by the mercury penetration porosimetry (Fig. 3a). Due to the intrusion principle, the nanopore volume measured by this method can be viewed as interconnected pore volume, which is accessed by the intruded mercury, convincingly demonstrating that the nanopores are interconnected. Furthermore, to preserve the nanopores as well as maintain appropriate mechanical strength, it is necessary to carefully select the sintering temperature. Generally, higher sintering temperature yields higher mechanical strength, however, the nanopores tend to close while the temperature is higher than 700°C [28]. Therefore, 700°C is chosen as the sintering temperature.

To examine the cells' in vitro response to our glass scaffold, cell morphology, survivability and number density were observed from deep interior of the scaffold by both SEM (Fig. 7) and confocal light microscopy (Figs. 5, 6). The results confirm that indeed the cells had migrated deep into the 3D scaffold, colonized the glass skeleton from inside, and adhered well to the glass surface. It is evident that osteoblast-like cells can migrate and penetrate deep into the interconnected pore meshwork of

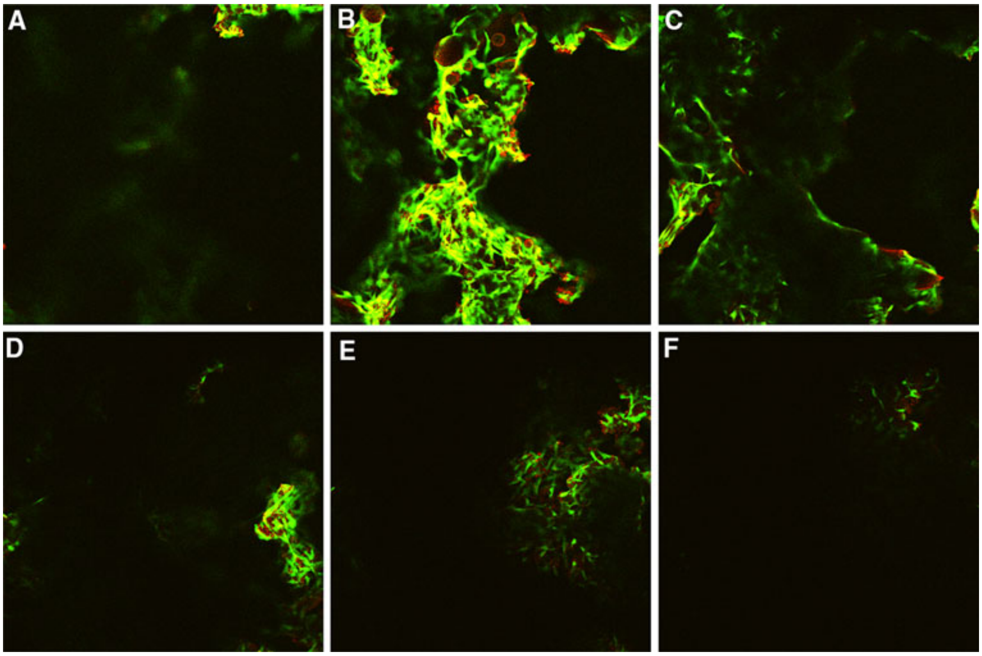

Fig. 5 Confocal microscope images of MG63 cells growing on and inside a BG scaffold acquired at different depth of **a** 0 μm, **b** 100 μm, **c** 200 μm, **d** 300 μm, **e** 400 μm, and **f** 500 μm. Cells were stained with Live/Dead Viability/Cytotoxicity staining. Living cells stain *green* and dead cells stain *red* (Color figure online)

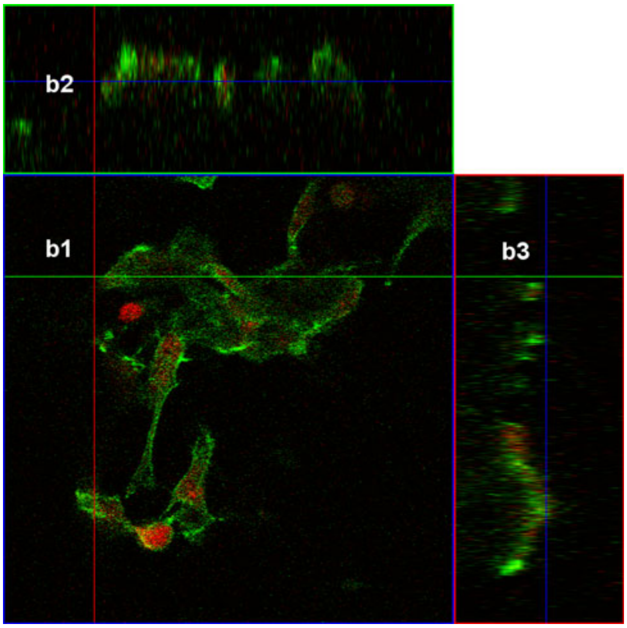

Fig. 6 Confocal microscope images of MG63 cells on and inside a glass scaffold. Cells were fixed with formaldehyde; F-actin was stained with Phalloidin Alexa 488 (*green*), and cell nuclei were stained with Propidium Iodide (*red*). *b1* is the image of a representative z-section in xy; *b2* (xz) and *b3* (yz) represent cross section images on z-planes where green and red lines locate respectively (Color figure online)

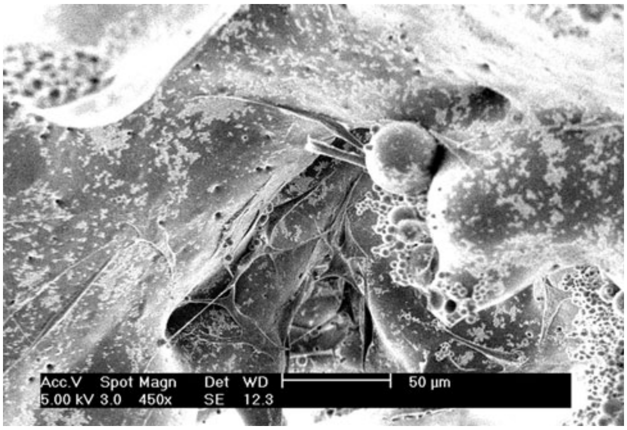

Fig. 7 SEM image of BG scaffold cross-section showing MG63 cells deep inside the macro-pores of a representative scaffold acquired 2 days post seeding

nano–macro porous BG scaffolds without encountering cytotoxic environments. In short, the nano-porosity, a prerequisite for an optimal dissolution rate of the scaffolds, does not appear to be harmful to cells as has been hypothesized earlier.

The above conclusions drawn from the response of cells to our nano–macro porous glass scaffold are further confirmed by in vivo response of animal tissue. This histological evaluation shows a high degree of biocompatibility of our newly developed scaffolds. Note the material-tissue interface, which indicates the scaffold's integration with no significant inflammatory response at the implanted site (shown in Fig. 8a). Positive response to the implanted scaffold is obvious from the remarkable angiogenesis in

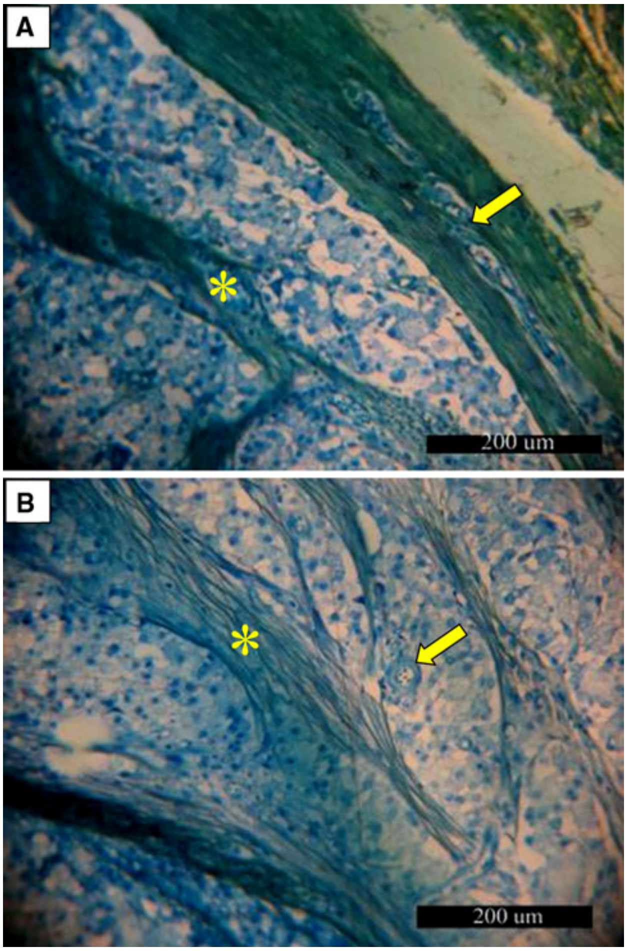

Fig. 8 Microphotographs showing the histological results of nano–macro porous bioactive glass discs subcutaneously implanted into a rabbit 5 weeks postoperatively. **a** A thin fibrous capsule can be detected surrounding the implanted material (*greenish* band in the area of the *arrow*). New vascularization formed within the fibrous tissue band of the capsule (*arrow*). Connective tissue strands are also extending from the periphery around the scaffold invading toward its core (*asterisk*). **b** The invading collagen fiber strands (*asterisk*) are distributed throughout the scaffold material showing high cellularity as well as new blood vessel formation (*arrow*) (Color figure online)

and around the fibrous tissue capsule as well as toward the core of the scaffold. These findings are supported by previous reports [45–47] that the presence of bioactive glass powder in vivo enhances new vascularization. This feature is a crucial step to initiate adequate wound healing and tissue regeneration. Furthermore, the widely distributed collagen fiber strands through the whole thickness of the scaffold associated with the high cellular components (shown in Fig. 8b) are evidence of regenerative tissue response to the chemical and physical structure of our newly designed bioactive glass scaffold.

Signs of desired biodegradation can be also observed as the scaffold gradually reduces to small isolated pieces surrounded with new vascularization as well as high cellular penetration, which are distributed throughout the whole region (not shown). Biodegradation of the nano–macro porous scaffold material and the observed high cellularity demonstrate the strong potential of this multi-scale porous material for enhancing the recruitment and proliferation of cells for new tissue formation, that gradually replace the dissolving bioactive glass.

5 Conclusions

Nano–macro bimodal sol–gel-derived glass scaffolds have been synthesized by a sol–gel-cum-spinodal decomposition process. Interconnected nanopores, with a diameter ranging from several to tens of nanometers and a modal value of 30 nm, coexist with interconnected macropores (tens to one hundred microns in diameter) in the BG scaffolds. Within 2 days post-seeding, MG63 osteoblast-like cells migrate and penetrate >500 micrometer deep into the bioscaffold without any indication of cytotoxic effects. They also exhibit excellent adhesion to the bioscaffold surface.

The results do not support the hypothesis that the environment within such tailored amorphous multi-porous (TAMP) bioscaffolds would be too hostile, hampering the survival of cultured cells. In vivo animal experiments provide initial evidences of the formation of new tissue with both blood vessels and collagen fibers deep inside the implanted scaffolds with no obvious inflammatory reaction. Such high viability of cells and new tissue formation indicate the potential use of recently developed nano–macro dual-porous bioactive glass as a novel and superior 3D scaffold for regenerative medicine as well as hard tissue engineering.

Acknowledgments We thank the National Science Foundation for supporting this work via International Materials Institute for New Functionality in Glass (DMR-0409588 and 0844014) and Materials World Network (DMR-0602975) programs, and The Howard Hughes Medical Institute (HHMI) for repeated Biosystems Dynamics Summer Institute grants. The work in the laboratory of MMF is supported by National Institutes of Health (NIH-NIGMS) grant R01 GM55725.

Conflict of interest There was no conflict of interest in conducting the work reported in this manuscript.

References

1. Merrill C, Elixhauser A. Hospital stays involving musculoskeletal procedures, healthcare cost and utilization project. Statistical Brief #34; 2007.
2. Griffon DJ. Evaluation of osteoproductive biomaterials: allograft, bone inducing agent, bioactive glass, and ceramics. Helsinki: University of Helsinki; 2002.

3. Hench LL. Bioceramics—from concept to clinic. J Am Ceram Soc. 1991;74(7):1487–510.
4. Hench LL. Bioceramics. J Am Ceram Soc. 1998;81(7):1705–28.
5. Hench LL. Biomaterials: a forecast for the future. Biomaterials. 1998;19(16):1419–23.
6. Pereira MM, Jones JR, Hench LL. Bioactive glass and hybrid scaffolds prepared by sol–gel method for bone tissue engineering. Adv Appl Ceram. 2005;104(1):35–42.
7. Hutmacher DW. Scaffolds in tissue engineering bone and cartilage. Biomaterials. 2000;21(24):2529–43.
8. Rezwan K, Chen QZ, Blaker JJ, Boccaccini AR. Biodegradable and bioactive porous polymer/inorganic composite scaffolds for bone tissue engineering. Biomaterials. 2006;27(18):3413–31. doi:10.1016/j.biomaterials.2006.01.039.
9. Freyman TM, Yannas IV, Gibson LJ. Cellular materials as porous scaffolds for tissue engineering. Prog Mater Sci. 2001;46(3–4):273–82.
10. Griffith LG. Emerging design principles in biomaterials and scaffolds for tissue engineering. In: Sipe JD, Kelley CA, McNicol LA, editors. Reparative medicine: growing tissues and organs. Annals of the New York Academy of Sciences; 2002. p. 83–95.
11. Jones JR, Lee PD, Hench LL. Hierarchical porous materials for tissue engineering. Philos Trans R Soc A-Math Phys Eng Sci. 2006;364(1838):263–81. doi:10.1098/rsta.2005.1689.
12. Karageorgiou V, Kaplan D. Porosity of 3d biomaterial scaffolds and osteogenesis. Biomaterials. 2005;26(27):5474–91. doi:10.1016/j.biomaterials.2005.02.002.
13. Chen QZZ, Thompson ID, Boccaccini AR. 45s5 bioglass (r)-derived glass–ceramic scaffolds for bone tissue engineering. Biomaterials. 2006;27(11):2414–25. doi:10.1016/j.biomaterials.2005.11.025.
14. Ramay HR, Zhang MQ. Preparation of porous hydroxyapatite scaffolds by combination of the gel-casting and polymer sponge methods. Biomaterials. 2003;24(19):3293–302. doi:10.1016/s0142-9612(03)00171-6.
15. Fu Q, Rahaman MN, Bal BS, Brown RF, Day DE. Mechanical and in vitro performance of 13–93 bioactive glass scaffolds prepared by a polymer foam replication technique. Acta Biomater. 2008;4(6):1854–64. doi:10.1016/j.actbio.2008.04.019.
16. Vitale-Brovarone C, Baino F, Verne E. High strength bioactive glass–ceramic scaffolds for bone regeneration. J Mater Sci-Mater Med. 2009;20(2):643–53. doi:10.1007/s10856-008-3605-0.
17. Michna S, Wu W, Lewis JA. Concentrated hydroxyapatite inks for direct-write assembly of 3D periodic scaffolds. Biomaterials. 2005;26(28):5632–9. doi:10.1016/j.biomaterials.2005.02.040.
18. Simon JL, Michna S, Lewis JA, Rekow ED, Thompson VP, Smay JE, et al. In vivo bone response to 3d periodic hydroxyapatite scaffolds assembled by direct ink writing. J Biomed Mater Res Part A. 2007;83A(3):747–58. doi:10.1002/jbm.a.31329.
19. Kaufmann E, Ducheyne P, Shapiro IM. Evaluation of osteoblast response to porous bioactive glass (45s5) substrates by RT-PCR analysis. Tissue Eng. 2000;6(1):19–28.
20. Livingston T, Ducheyne P, Garino J. In vivo evaluation of a bioactive scaffold for bone tissue engineering. J Biomed Mater Res. 2002;62(1):1–13. doi:10.1002/jbm.10157.
21. Liang W, Rahaman MN, Day DE, Marion NW, Riley GC, Mao JJ. Bioactive borate glass scaffold for bone tissue engineering. J Non-Cryst Solids. 2008;354(15–16):1690–6. doi:10.1016/j.jnoncrysol.2007.10.003.
22. Liang W, Wang M, Day DE, Russel C. Sodium silicate bonded borate glass scaffolds for tissue engineering. J Mater Sci. 2007;42(24):10138–42. doi:10.1007/s10853-007-2101-0.
23. Rahaman MN, Fu Q, Day DE, Bal BS. In vitro evaluation of hydroxyapatite and bioactive glass (13–93) scaffolds prepared by unidirectional freezing of suspensions. In: 33rd international conference on advanced ceramics and composites (ICACC), Daytona Beach, FL; 2009.
24. Brown RF, Day DE, Day TE, Jung S, Rahaman MN, Fu Q. Growth and differentiation of osteoblastic cells on 13–93 bioactive glass fibers and scaffolds. Acta Biomater. 2008;4(2):387–96. doi:10.1016/j.actbio.2007.07.006.
25. Elias KL, Price RL, Webster TJ. Enhanced functions of osteoblasts on nanometer diameter carbon fibers. Biomaterials. 2002;23(15):3279–87.
26. Woo KM, Chen VJ, Ma PX. Nano-fibrous scaffolding architecture selectively enhances protein adsorption contributing to cell attachment. J Biomed Mater Res Part A. 2003;67A(2):531–7. doi:10.1002/jbm.a.10098.
27. Dalby MJ, Gadegaard N, Tare R, Andar A, Riehle MO, Herzyk P, et al. The control of human mesenchymal cell differentiation using nanoscale symmetry and disorder. Nat Mater. 2007;6(12):997–1003. doi:10.1038/nmat2013.
28. Jones JR, Ehrenfried LM, Hench LL. Optimising bioactive glass scaffolds for bone tissue engineering. Biomaterials. 2006;27(7):964–73. doi:10.1016/j.biomaterials.2005.07.017.
29. Marques AC, Jain H, Almeida RM. Sol–gel derived nano/macroporous scaffolds. Phys Chem Glasses-Eur J Glass Sci Technol Part B. 2007;48(2):65–8.
30. Marques AC, Almeida RM, Thiema A, Wang SJ, Falk MM, Jain H. Sol–gel-derived glass scaffold with high pore interconnectivity and enhanced bioactivity. J Mater Res. 2009;24(12):3495–502. doi:10.1557/jmr.2009.0440.
31. Marques AC, Jain H, Kiely C, Song K, Kiely CJ, Almeida RM. Nano/macroporous monolithic scaffolds prepared by the sol–gel method. J Sol–Gel Sci Technol. 2009;51(1):42–7. doi:10.1007/s10971-009-1960-z.
32. Jones JR, Tsigkou O, Coates EE, Stevens MM, Polak JM, Hench LL. Extracellular matrix formation and mineralization on a phosphate-free porous bioactive glass scaffold using primary human osteoblast (hob) cells. Biomaterials. 2007;28(9):1653–63. doi:10.1016/j.biomaterials.2006.11.022.
33. Gough JE, Jones JR, Hench LL. Nodule formation and mineralisation of human primary osteoblasts cultured on a porous bioactive glass scaffold. Biomaterials. 2004;25(11):2039–46. doi:10.1016/j.biomaterials.2003.07.001.
34. Brunauer S, Emmett PH, Teller E. Adsorption of gases in multimolecular layers. J Am Chem Soc. 1938;60(2):309–19. doi:10.1021/ja01269a023.
35. Barrett EP, Joyner LG, Halenda PP. The determination of pore volume and area distributions in porous substances. 1. Computations from nitrogen isotherms. J Am Chem Soc. 1951;73(1):373–80.
36. National Research Council. Guide for the care and use of laboratory animals. 2nd ed. Washington, DC: National Academy Press, Institute of Laboratory Animal Resources; 1996. p. 56–76.
37. Marei MK, Nouh SR, Saad MM, Ismail NS. Preservation and regeneration of alveolar bone by tissue-engineered implants. Tissue Eng. 2005;11(5–6):751–67.
38. James KS, Zimmerman MC, Kohn J. Small animal surgical and histological procedures for characterizing the performance of tissue-engineered bone grafts. In: Tissue engineering methods and protocols. Methods in molecular medicine. Humana Press; 1999. p. 121–31.
39. Hench LL, West JK. The sol–gel process. Chem Rev. 1990;90(1):33–72.
40. Nakanishi K. Pore structure control of silica gels based on phase separation. J Porous Mater. 1997;4:67.
41. Nakanishi K, Takahashi R, Nagakane T, Kitayama K, Koheiya N, Shikata H, et al. Formation of hierarchical pore structure in silica gel. J Sol–Gel Sci Technol. 2000;17(3):191–210.

42. Takahashi R, Nakanishi K, Soga N. Effects of aging and solvent exchange on pore structure of silica-gels with interconnected macropores. J Non-Cryst Solids. 1995;189(1–2):66–76.
43. Nakanishi K, Komura H, Takahashi R, Soga N. Phase-separation in silica sol–gel system containing poly(ethylene oxide). 1. Phase relation and gel morphology. Bull Chem Soc Jpn. 1994;67(5): 1327–35.
44. Lin S, Ionescu C, Pike KJ, Smith ME, Jones JR. Nanostructure evolution and calcium distribution in sol–gel derived bioactive glass. J Mater Chem. 2009;19(9):1276–82. doi:10.1039/b814292k.
45. Day RM. Bioactive glass stimulates the secretion of angiogenic growth factors and angiogenesis in vitro. Tissue Eng. 2005; 11(5–6):768–77.
46. Leu A, Stieger SM, Dayton P, Ferrara KW, Leach JK. Angiogenic response to bioactive glass promotes bone healing in an irradiated calvarial defect. Tissue Eng Part A. 2009;15(4): 877–85. doi:10.1089/ten.tea.2008.0018.
47. Gorustovich AA, Roether JA, Boccaccini AR. Effect of bioactive glasses on angiogenesis: a review of in vitro and in vivo evidences. Tissue Eng Part B. 2010;16:199–207.